The Astrophysical Journal, 985:83 (11pp), 2025 May 20 https://doi.org/10.3847/1538-4357/adc4c3


# Metallicity Scatter Originating from Subkiloparsec Starbursting Clumps in the Core of a Protocluster at $z = 7.88$

Takahiro Morishita[1], Massimo Stiavelli[2,3,4], Eros Vanzella[5], Pietro Bergamini[5,6], Kristan Boyett[7], Marco Chiaberge[4,8], Claudio Grillo[6,9], Nicha Leethochawalit[10], Matteo Messa[5], Guido Roberts-Borsani[11,12], Piero Rosati[5,13], and Anowar J. Shajib[14,15,16,17]

[1] IPAC, California Institute of Technology, MC 314-6, 1200 E. California Boulevard, Pasadena, CA 91125, USA; takahiro@ipac.caltech.edu
[2] Space Telescope Science Institute, 3700 San Martin Drive, Baltimore, MD 21218, USA
[3] Department of Astronomy, University of Maryland, College Park, MD 20742, USA
[4] The William H. Miller III Department of Physics and Astronomy, Johns Hopkins University, Baltimore, MD 21218, USA
[5] INAF—OAS, Osservatorio di Astrofisica e Scienza dello Spazio di Bologna, via Gobetti 93/3, I-40129 Bologna, Italy
[6] Dipartimento di Fisica, Università degli Studi di Milano, Via Celoria 16, I-20133 Milano, Italy
[7] Department of Physics, University of Oxford, Denys Wilkinson Building, Keble Road, Oxford, OX1 3RH, UK
[8] Space Telescope Science Institute for the European Space Agency (ESA), ESA Office, 3700 San Martin Drive, Baltimore, MD 21218, USA
[9] INAF—IASF Milano, via A. Corti 12, I-20133 Milano, Italy
[10] National Astronomical Research Institute of Thailand (NARIT), Mae Rim, Chiang Mai, 50180, Thailand
[11] Department of Astronomy, University of Geneva, Chemin Pegasi 51, 1290 Versoix, Switzerland
[12] Department of Physics & Astronomy, University College London, London, WC1E 6BT, UK
[13] Dipartimento di Fisica e Scienze della Terra, Università degli Studi di Ferrara, Via Saragat 1, I-44122 Ferrara, Italy
[14] Department of Astronomy and Astrophysics, University of Chicago, Chicago, IL 60637, USA
[15] Kavli Institute for Cosmological Physics, University of Chicago, Chicago, IL 60637, USA
[16] Center for Astronomy, Space Science and Astrophysics, Independent University, Bangladesh, Dhaka 1229, Bangladesh
*Received 2025 January 20; revised 2025 March 1; accepted 2025 March 19; published 2025 May 15*

## Abstract

We present new JWST NIRSpec integral field unit (IFU) G395H/F290LP observations of a merging galaxy system at $z = 7.88$, part of A2744-z7p9OD, the most distant protocluster to date. The IFU cube reveals [O III]$_{\lambda5007}$ emissions in two previously known galaxies, ZD3 and ZD6, and a newly identified galaxy, ZD12, at $z_{\rm spec} = 7.8762$. One of the detected [O III]-emitting regions has a detection of the auroral [O III]$_{\lambda4363}$ line, allowing us to derive a direct metallicity of $\log({\rm O/H}) + 12 = 7.4 \pm 0.2$, while metallicities in other regions are measured using strong-line calibration methods. We find large deviations within the measured metallicity ($\Delta \log({\rm O/H}) \sim 1$), which suggests a fast chemical enrichment from intense star formation and merger-driven growth, as expected in early galaxies. Our analysis shows that metal-poor regions could easily be outshone by more enriched regions, posing a challenge for spectroscopic analysis based on integrated light (i.e., NIRSpec/MSA) against identifying metal-free star formation in the early Universe. NIRCam imaging reveals seven UV-bright clumps in ZD12, in a stellar mass range of $\log M_*/M_\odot \sim 7.6$–$8.9$. Four of them are unresolved ($\lesssim$100 pc) and intensely star-forming ($>30\,M_\odot\,{\rm yr}^{-1}\,{\rm kpc}^{-2}$), likely contributing to the scatter in metallicity by producing an ideal environment for rapid chemical cycles. Lastly, we revisit the nature of the host protocluster by including new member galaxies identified here and in the literature, and obtain a local overdensity factor $\delta = 44^{+89}_{-31}$, a total halo mass $M_{\rm h} = 5.8^{+0.2}_{-0.3} \times 10^{11}\,M_\odot$, and a formal velocity dispersion $1100 \pm 500\,{\rm km\,s}^{-1}$.

*Unified Astronomy Thesaurus concepts:* Active galaxies (17); Metallicity (1031); High-redshift galaxy clusters (2007); Star formation (1569)

## 1. Introduction

The gas cycle within a galaxy system plays an important role in shaping the host structure and establishing its observed properties. The ejecta from previously formed stars enrich surrounding gas, some of which contribute to subsequent star formation cycles, and enhance chemical abundances within the system. Galaxies are by no means closed systems: A series of interplays with other galaxies and the cosmic web through the accretion of pristine gas adds further complications in establishing the chemical enrichment journey over the lifetime of a galaxy (e.g., B. D. Oppenheimer & R. Davé 2006; J. Tumlinson et al. 2017; J. Chisholm et al. 2018).

Despite such complexities, the accumulation of stars evolved in such a cyclical way represents a major component of galaxies in later epochs, culminating with an established relation of metal contents and other fundamental galaxy properties, such as stellar mass, i.e., the mass–metallicity relation, seen in the local Universe (e.g., C. A. Tremonti et al. 2004; A. Gallazzi et al. 2005; B. H. Andrews & P. Martini 2013; E. N. Kirby et al. 2013; M. Curti et al. 2020). Studies, enabled by the JWST, have extended the investigation to higher redshifts. The correlation between the two parameters seems to exist beyond the local Universe, to $z > 3$ (M. Curti et al. 2024; K. Nakajima et al. 2023; R. L. Sanders et al. 2024; I. Chemerynska et al. 2024; I. H. Laseter et al. 2024), but with an offset to the local relation (e.g., K. E. Heintz et al. 2023; T. Morishita et al. 2024a). Studying the relationship in earlier times gives us insight into how different physical mechanisms

[17] NHFP Einstein Fellow.

act on the formation of the tight correlation (e.g., X. Ma et al. 2016; A. Pallottini et al. 2024).

In this regard, those early JWST observations of high-$z$ galaxies are already informative, finding considerably large scatter around the relation: at $z \sim 0$, the scatter is found to be $\sim$0.1 (M. Curti et al. 2020), while the observed scatter is significantly increased to $\gtrsim$0.3 dex at $z > 5$. T. Morishita et al. (2024a) investigated this in detail and discussed the possible origins. The study found that the scatter could not be reduced by the introduction of an additional parameter in the relationship, unlike the case for low-$z$ galaxies with star formation rate (SFR) as the third parameter (e.g., F. Mannucci et al. 2010). Instead, the scatter was found to be related to systematics coming from the limited slit size of NIRSpec/MSA and the exact slit position within the target galaxy. In addition, the same study argues that, given that many MSA observations put the slit in the photocenter of galaxies by default, the measured metallicity with NIRSpec/MSA may be biased toward a more enriched region. However, this explanation is possible only when there are significant metallicity variations within individual galaxies, which is not obvious in early galaxies, thus requiring further investigation with spatially resolved spectroscopy.

Recent studies using JWST integral field unit (IFU) observations have shown various conclusions. C. Marconcini et al. (2024a) found small metallicity variations ($\Delta \log \mathrm{O/H} \lesssim 0.2$ dex) within the luminous galaxy system CR7 at $z = 6.6$ (see also G. C. Jones et al. (2024) and J. Scholtz et al. (2025) for similar findings in COS-3018 at $z = 6.85$ and B14-65666 at $z = 7.152$, respectively). On the other hand, C. Marconcini et al. (2024b) reported larger deviations ($\gtrsim$0.5 dex) within MACS1149-JD1 at $z = 9.11$. Similarly, S. Arribas et al. (2024) found a large variation in metallicity, $\Delta \sim 0.8$ dex, within a massive, multiple-galaxy system at $z = 6.9$. The wealth of high-resolution data provided by the JWST now enables us to explore the physical mechanisms driving such deviations.

In this paper, we present a new $R \sim 3000$ IFU observation executed in JWST's Cycle 2 (PID 4553; M. Stiavelli et al. 2023) toward a unique merging galaxy system at $z = 7.88$. The system is located in the core of the most distant protocluster, A2744-z7p9OD, to date (N. Laporte et al. 2014; W. Zheng et al. 2014; M. Ishigaki et al. 2016; G. Roberts-Borsani et al. 2022; T. Hashimoto et al. 2023; T. Morishita et al. 2023). Furthermore, being behind the massive cluster Abell 2744, the system is magnified by a factor of $\mu \sim 2$, enabling us to study the interstellar medium (ISM) properties and subgalactic structures in great detail. In Section 2, we present our data reduction and analyses. In Section 3, we measure the physical properties of the identified member galaxies via emission-line analysis and spectral energy distribution (SED) fitting. In Section 4, we discuss the inferred properties of those galaxies in the context of the mass–metallicity relationship and provide updated characterizations of the host protocluster A2744-z7p9OD. Where relevant, we adopt the AB magnitude system (J. B. Oke & J. E. Gunn 1983; M. Fukugita et al. 1996), cosmological parameters of $\Omega_\mathrm{m} = 0.3$, $\Omega_\Lambda = 0.7$, $H_0 = 70\,\mathrm{km\,s^{-1}\,Mpc^{-1}}$, and the G. Chabrier (2003) initial mass function (IMF). Throughout the manuscript, we use the term metallicity to refer to oxygen abundance.

## 2. Data

### 2.1. NIRSpec IFU Observations and Reduction

Our NIRSpec IFU observations (GTO4553; PI: Stiavelli) were executed within a single visit on 2024 October 27, centered at (R.A., decl.) = (3.60680, −30.38082). The visit was configured at the V3 position angle PA_V3 = 41.°1 with the high-resolution grating G395H/F290LP. The exposure consists of 12 dithers, with a total science time of 19,432 s (7.44 hr including overhead was charged).

The data are reduced using the official JWST pipeline (v1.16.0) with additional custom steps. Briefly, we retrieve the level1 products (_uncal.fits) from MAST. We run the stage1 step and then the stage2 step, with additional stripe elimination using NSClean (J. R. Rigby et al. 2025)[18] and cosmic-ray (CR) rejection using `lacosmic` (P. G. van Dokkum 2001; L. Bradley 2023). We also run the source detection tool `SExtractor` (E. Bertin & S. Arnouts 1996) in each _rate image and flag significant point-like sources, i.e., CRs that are not detected in the previous steps. We run the stage3 step to construct a cube and subtract background in each wavelength frame using off-source regions. We run `lacosmic` again in each wavelength frame to mask any residual CRs.

### 2.2. Imaging Data and Photometry

We utilize the JWST NIRCam imaging data available in the field. These include GLASS-JWST (ERS1324; T. Treu et al. 2022), UNCOVER (GO2561; R. Bezanson et al. 2024), DD2756 (W. Chen et al. 2022), GO2883 (PI: F. Sun), All the Little Things (ALT; GO3516; R. P. Naidu et al. 2024), GO3538 (PI: E. Iani), BEACON (GO3990; T. Morishita et al. 2025), and Medium Bands, Mega Science (GO4111; K. A. Suess et al. 2024). We also utilize Hubble Space Telescope (HST) Advanced Camera for Surveys (ACS) and Wide Field Camera 3 IR mosaic images, made publicly available by the GLASS-JWST team (E. Merlin et al. 2022), which combined data from multiple HST programs (M. Postman et al. 2012; J. M. Lotz et al. 2017; P. L. Kelly et al. 2018; C. L. Steinhardt et al. 2020).

All data were compiled and used for photometry as described in T. Morishita et al. (2025). Briefly, we identified sources in the IR detection image (F277W+F356W+F444W stack) using `SExtractor` (E. Bertin & S. Arnouts 1996), and measured fluxes on the mosaic images (matched to the F444W point-spread function, PSF), with a fixed aperture of radius $r = 0.''16$. The measured fluxes are calibrated using the method introduced in T. Morishita & M. Stiavelli (2023). Interested readers are referred to the work for more details. The filters included in our analysis and the limiting magnitudes ($5\sigma$, for a point source) are as follows: HST F435W (28.7), F606W (28.1), F775W (28.3), F814W (27.7), F105W (27.5), F125W (27.5), F140W (28.2), and F160W (27.1); NIRCam F070W (28.5), F090W (28.9), F115W (28.7), F140M (27.9), F150W (28.8), F162M (27.9), F182M (28.1), F200W (28.9), F210M (28.0), F250M (28.0), F277W (29.1), F300M (28.1), F335M (28.1), F356W (29.1), F360M (28.2), F410M (28.6), F430M (27.7), F444W (28.9), F460M (26.8), and F480M (27.2); NIRISS F115W (28.8), F150W (28.7), F200W (28.6), F356W (28.8), F430M (27.6), F444W (28.5), and F480M (27.0).

[18] https://github.com/JWST-Templates/NSClean

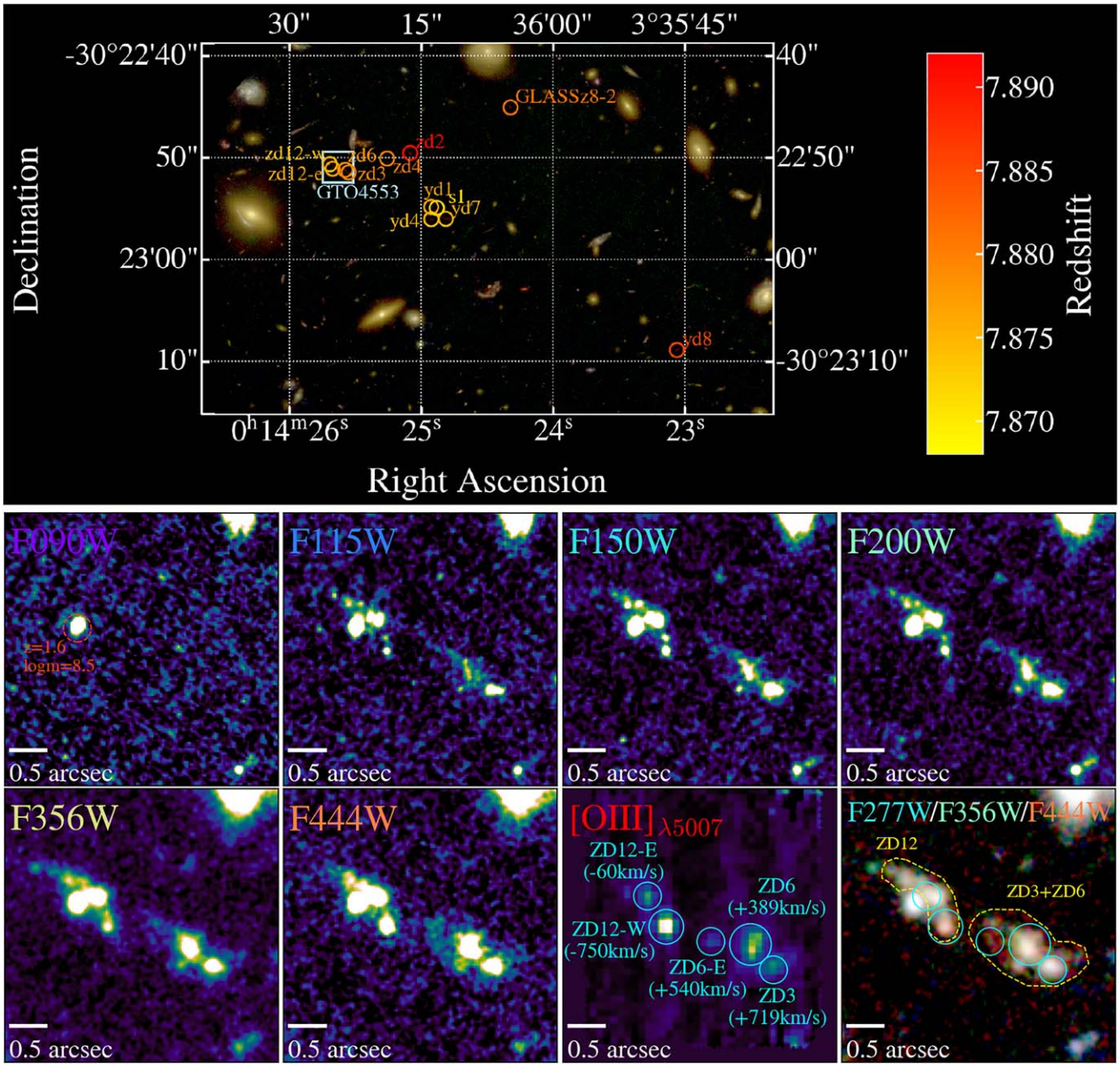


**Figure 1.** Top: mosaic image of the field (blue: HST/ACS F435W; green: NIRCam F090W; red: NIRCam F150W) centered on the protocluster A2744-z7p9OD. The spectroscopically confirmed members are marked (circles). The field of view of our IFU observations GTO4553 is shown (blue rectangles). Bottom: postage stamps of NIRCam images ($4'' \times 4''$), showing the region of the GTO4553 observations. Five [O III]-emitting regions analyzed in the main texts are marked in the $[\mathrm{O\,III}]_{\lambda5007}$ line map (cyan circles) with the velocity offset measurement from the systemic redshift $z_{\rm sys} = 7.8784$.

In the following analysis, we adopt the latest magnification model by P. Bergamini et al. (2023a, 2023b).

## 3. Analysis and Results

### 3.1. Emission-line Analysis

Emission lines are extracted using the flux cube reduced in Section 2.1. Given the limited signal-to-noise ratio (SNR), we mainly base our analysis on the strongest emission line, $[\mathrm{O\,III}]_{\lambda5007}$. We extract the $[\mathrm{O\,III}]_{\lambda5007}$ emission-line map by coadding cube frames (each weighted by the corresponding rms frame) over the velocity range $\pm 300\,\mathrm{km\,s^{-1}}$ centered at $z = 7.88$, i.e., the systemic redshift of ZD3 and ZD6.

In Figure 1, we show the extracted $[\mathrm{O\,III}]_{\lambda5007}$ emission-line map along with the NIRCam images. We identify five separate regions detected with SNR $> 3$. Two are ZD3 and ZD6, previously spectroscopically confirmed galaxies (T. Morishita et al. 2023). In addition, one emitting region is detected east of ZD6, hereafter referred to as ZD6-E. Two strong [O III]-emitting regions are identified within the eastern system ZD12,[19] which we refer to as ZD12-W and ZD12-E, respectively. In what follows, we base our analysis on those five regions. We refer to them as *[O III]-emitting regions* to

[19] W. Zheng et al. (2014) presented 11 $z$-band dropout sources. ZD12 was not identified in the original photometric study, possibly due to confusion with the foreground galaxy.

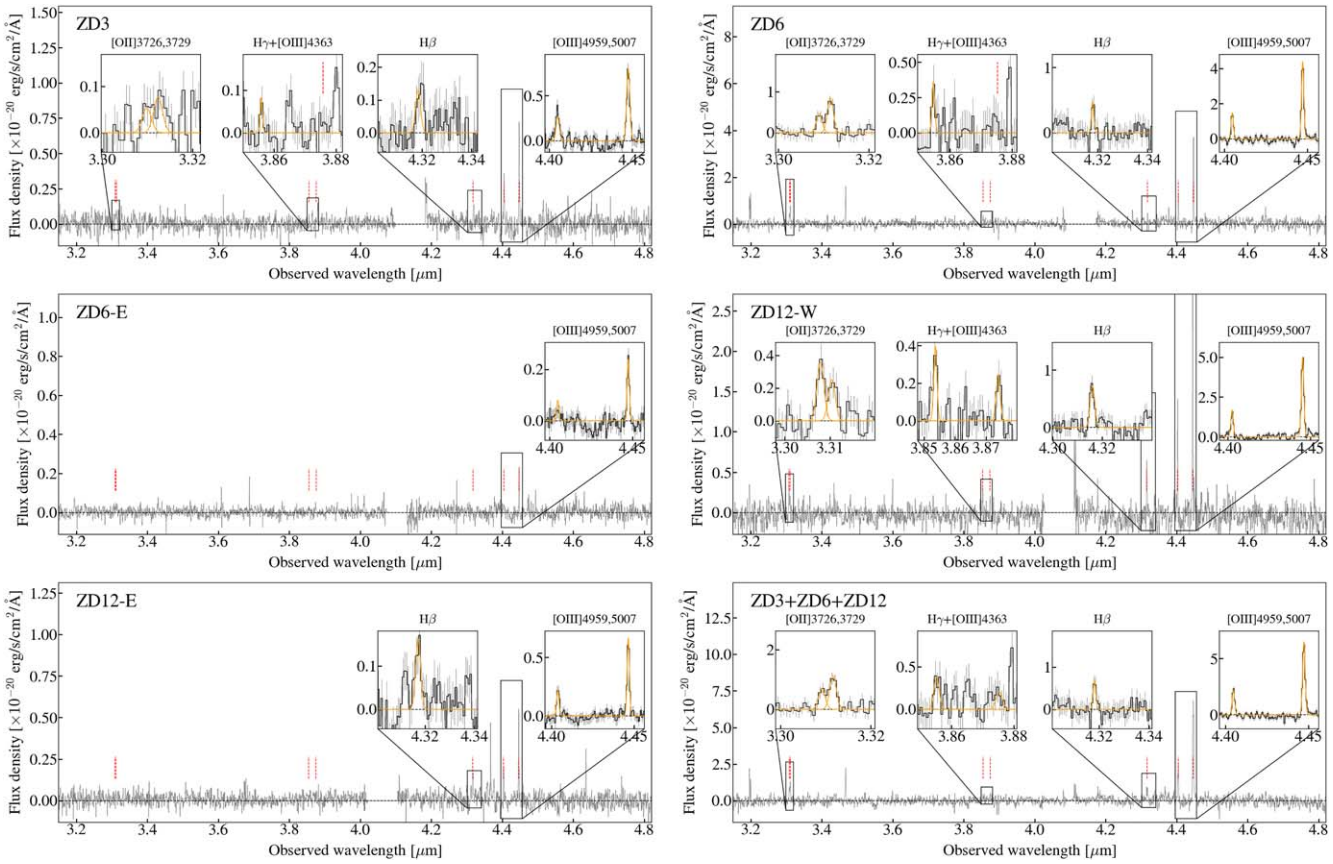


**Figure 2.** Extracted G395H/F290LP spectra of the [O III]-emitting regions (black lines). The defined regions for each spectrum are shown in Figure 1. Detected emission lines (SNR $>$ 1.5) are shown in the inset, where the fitted Gaussian models (orange) are shown.

distinguish them from UV *clumps*, which are defined separately later in this paper. The entire emitting region extends for ∼2.″9 in the sky, or ∼7.2 kpc in the source plane.

Spectra are extracted within apertures of ∼0.″15–0.″3 centered on the [O III]-emitting region, where the aperture size is determined by a growth curve method. Furthermore, we define larger segments for the entire ZD3+ZD6, ZD12, and ZD3+ZD6+ZD12 systems (regions refined by yellow lines in Figure 1) and extract the spectra for further analysis. The extracted spectrum of the total system is shown in Figure 2.

We note a foreground galaxy (ID 51545; 00:14:25.7, –30:22:50.6), to the southeast of ZD12 (Figure 1). This galaxy is clearly detected in the F090W image and thus is not a $z$-band dropout source; instead, the galaxy has a photometric redshift solution of $z \sim 1.6$ and is best fitted with a star-forming galaxy template ($\log M_*/M_\odot \sim 8.5$), while our IFU cube does not reveal strong emission lines.

We fit each emission line of interest with a Gaussian function. Our basic strategy is to define a wavelength window for each line, model the underlying continuum spectrum (either source origin or residual background) by a polynomial fit, and subtract it from the one-dimensional spectrum before the Gaussian fit is carried out. The model includes amplitude, line-width, and redshift parameters. The [O III]$_{\lambda\lambda 4959+5007}$ doublet lines are modeled with a fixed line ratio (1:3), with common line-width and redshift parameters. The [O II]$_{\lambda\lambda 3726+3729}$ doublet lines are modeled with a common line width, but without their line ratio fixed (see Section 3.2). For emission lines other than those two doublet pairs, we fix the redshift parameter to the value determined by the [O III] doublets and leave the amplitude and width as free parameters.

The flux of each line is measured by integrating the modeled Gaussian component, and the flux error is estimated by summing the error weighted by the amplitude of the Gaussian model in quadrature. The uncertainty associated with the modeled continuum is also added. In the following analysis, we adopt flux measurements when the line is detected (SNR $\geqslant$ 1.5); for those not detected, we proceed with our analysis using the 1.5$\sigma$ upper limit. We securely detect the [O III] doublets in all regions, H$\beta$ in four, and [O II] in three. In addition, the auroral [O III]$_{\lambda 4363}$ is detected in ZD12-W, allowing us to measure the electron temperature (Section 3.2).

We find that all five regions are within a small distance along the radial direction ($\Delta v = 1500\,\mathrm{km\,s^{-1}}$). The separation between ZD3 and ZD6 is even smaller, $\Delta v = 350\,\mathrm{km\,s^{-1}}$, confirming that they are interacting, rather than by chance alignment in the sky plane. On the other hand, ZD12-E and ZD12-W have a greater velocity offset, $\Delta v \sim 700\,\mathrm{km\,s^{-1}}$. Although the two regions are not deblended in our photometric analysis, they may remain two isolated galaxy systems.

The measured line fluxes are corrected for dust attenuation. Although it is ideal to determine the correction on the basis of the ratio of Balmer lines, no more than one line is confidently detected in our cube, except for ZD12-W. We thus apply the correction derived from our resolved SED analysis (Section 3.3) after rescaling it by a factor of 2.27 (D. Calzetti et al. 2000; see also T. Morishita et al. 2024b, which found the assumption is valid using $z > 3$ galaxies) that accounts for

**Table 1**
Dust-corrected Line Fluxes

| ID | [O II]$_{3726}$ | [O II]$_{3729}$ | H$\gamma_{4340}$ | [O III]$_{4363}$ | H$\beta_{4861}$ | [O III]$_{4959,5007}$ |
|---|---|---|---|---|---|---|
| ZD3 | 2.9 ± 1.7 | 4.3 ± 1.8 | 1.6 ± 1.0 | < 1.8 | 6.5 ± 2.4 | 50.4 ± 9.0 |
| ZD6 | 40.2 ± 10.4 | 75.5 ± 11.5 | 18.2 ± 7.0 | < 13.3 | 22.8 ± 7.7 | 382.8 ± 32.6 |
| ZD6-E | <1.7 | <1.8 | <1.3 | <1.2 | <1.1 | 13.3 ± 4.4 |
| ZD12-W | 20.7 ± 4.3 | 14.7 ± 4.7 | 14.0 ± 3.1 | 10.4 ± 3.0 | 40.5 ± 5.5 | 313.9 ± 21.0 |
| ZD12-E | <1.3 | 1.8 ± 0.8 | <0.7 | <0.9 | 6.9 ± 1.3 | 26.1 ± 4.3 |
| ZD3+ZD6 | 44.0 ± 10.8 | 72.6 ± 11.8 | 24.5 ± 9.2 | 15.8 ± 9.8 | 26.8 ± 7.8 | 456.4 ± 36.4 |
| ZD12 | 20.1 ± 6.2 | 17.0 ± 5.8 | 11.7 ± 2.9 | 15.4 ± 4.6 | 60.9 ± 7.8 | 429.4 ± 29.6 |
| ZD3+ZD6+ZD12 | 53.3 ± 14.1 | 74.6 ± 12.8 | 27.6 ± 11.2 | 33.1 ± 11.1 | 60.9 ± 12.6 | 706.6 ± 51.4 |

**Note.** Fluxes are in Units of $10^{-20}$ erg s cm$^{-2}$. Flux errors are 1$\sigma$. 1.5$\sigma$ upper limits are quoted for nondetected lines (SN < 1.5).

continuum and emission-line dust effects. Dust-corrected line fluxes are reported in Table 1.

### 3.2. Metallicity Measurements

#### 3.2.1. ZD12-W: Electron Temperature, Density, and Direct Oxygen Abundance

Our data cube reveals the detection of [O III]$_{\lambda4363}$ in ZD12-W. The auroral line provides a reliable method to derive the electron temperature and from that the oxygen metallicity, known as the direct-T method (e.g., Y. I. Izotov et al. 2006). Therefore, while we rely on a strong-line calibration method for other [O III]-emitting regions, we derive the direct metallicity for ZD12-W for comparison.

The direct method requires knowledge of the electron density $n_e$, which can be measured by the flux ratio of the [O II] doublet lines. The line ratio is measured as $I_{3729}/I_{3726} = 0.71 \pm 0.27$, where $I$ represents the corresponding line intensity. To obtain the electron temperature $T_e$ and the electron density $n_e$, we follow Y. I. Izotov et al. (2006) and solve the following equations iteratively:

$$n_e = \frac{(c\, I_{3729}/I_{3726} - a\, b)}{(a - I_{3729}/I_{3726})}\left(\frac{T_e}{10^4}\right)^{-1/2}, \quad (1)$$

and

$$\frac{I_{4959+5007}}{I_{4363}} = \frac{7.90\exp(3.29 \times 10^4/T_e)}{1 + 4.5 \times 10^{-4} n_e/T_e^{1/2}}, \quad (2)$$

where $a = 0.3771$, $b = 2468$, and $c = 638.4$ from R. L. Sanders et al. (2016). We note that the temperature term is added to the first equation by following D. E. Osterbrock (1989). We obtain the electron temperature of $O^{++}$, $T_e = 2.4^{+0.7}_{-0.4} \times 10^4$ K, and $n_e = 2200^{+6700}_{-1600}$ cm$^{-3}$. The larger error bar of the upper-bound density is due to the fact that the adopted equation has a much steeper slope at $n_e \gtrsim 1000$ cm$^{-3}$ (i.e., $I_{3729}/I_{3726} \lesssim 0.5$). The measured density is high, but not exceptional among high-$z$ galaxies studied with JWST (e.g., Y. Isobe et al. 2023; P. Senchyna et al. 2024; Abdurro'uf et al. 2024; S. Li et al. 2025; M. W. Topping et al. 2024), as shown in Figure 3. Interestingly, ZD6, the only other source that has a robust doublet measurement, shows a very high line ratio, $I_{3729}/I_{3726} = 1.88 \pm 0.50$. This leads us to $n_e \lesssim 40$ cm$^{-3}$ assuming $T_e = 10^4$ K, exhibiting a stark contrast to the one measured for ZD12-W. Similarly, using the line flux measured in the total (ZD3+ZD6+ZD12) spectrum, we obtain $n_e \lesssim 430$ cm$^{-3}$.

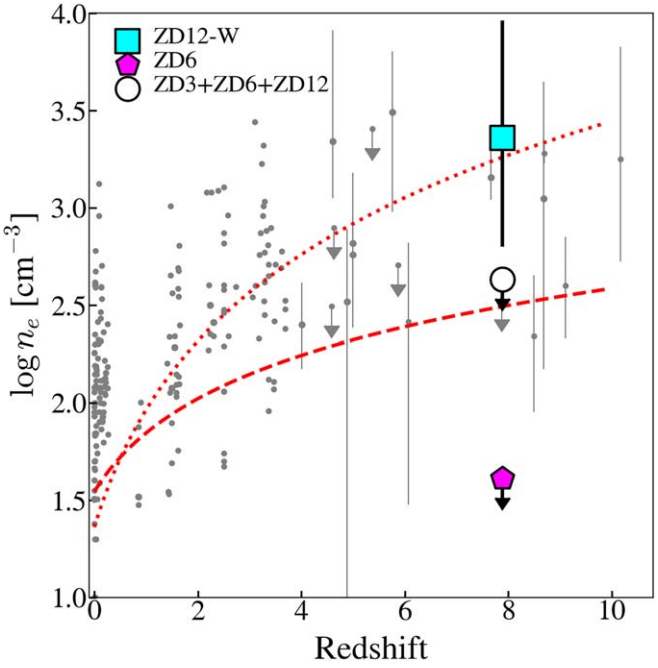


**Figure 3.** Electron density measurements of ZD12-W (cyan square), ZD6 (magenta pentagon), and the total ZD3+ZD6+ZD12 (white circle) shown along with those in the literature (gray dots; data compiled in Abdurro'uf et al. 2024). The evolution curves ($\propto (1+z)$ and $\propto (1+z)^2$) derived in Y. Isobe et al. (2023) are shown.

We then estimate the $O^+$ temperature from the $O^{++}$ temperature as $1.5 \times 10^4$ K by following D. E. Osterbrock (1989). The elemental abundances of $O^{++}$ and $O^+$ are derived by using the relation in Y. I. Izotov et al. (2006), and we obtain $\log(O/H) + 12 = 7.41^{+0.19}_{-0.17}$. We examined the effect of the density uncertainty by adopting $n_e = 1$ cm$^{-3}$ and 10,000 cm$^{-3}$, and indeed found that the variability of the result stays within the uncertainties quoted.

#### 3.2.2. Oxygen Abundance via Strong-line Calibration Method

For other [O III]-emitting regions that do not detect [O III]$_{\lambda4363}$, we use a strong-line calibration method to derive metallicity. We use the formula presented in R. L. Sanders et al. (2024), which offers calibration by using the sample of $z = 2$–9 galaxies equipped with direct-T metallicity measurements. We combine two line calibrators, $R3 = \log([O\,III]_{\lambda5007}/H\beta)$ and $R23 = \log(([O\,III]_{\lambda\lambda4959,5007} + [O\,II]_{\lambda\lambda3726,3729})/H\beta)$, and obtain $\log(O/H)$, similar to M. Curti et al. (2024) and I. Lamperti et al. (2024). In this study, we provide the R23 and R3

**Table 2**
Physical Properties of [O III]-emitting Regions

| ID | R.A. (deg) | Decl. (deg) | $z$ | $\mu$ | $M_{\rm UV}$ (mag) | log $M_*$ ($M_\odot$) | logSFR$_{\rm UV}$ ($M_\odot$ yr$^{-1}$) | log(O/H) +12 | log$\xi_{\rm ion}$ (Hz erg$^{-1}$) | EW$_0$([O III]) (Å) |
|---|---|---|---|---|---|---|---|---|---|---|
| ZD3 | 3.6064713 | −30.3810350 | 7.8808 | $1.96^{+0.07}_{-0.06}$ | $-18.5^{+0.1}_{-0.1}$ | $7.9^{+0.1}_{-0.1}$ | $0.4^{+0.1}_{-0.1}$ | 7.64 ± 0.20 | $25.3^{+0.1}_{-0.2}$ | $167^{+31}_{-31}$ |
| ZD6 | 3.6065784 | −30.3809330 | 7.8797 | $1.96^{+0.07}_{-0.06}$ | $-19.5^{+0.1}_{-0.1}$ | $8.3^{+0.1}_{-0.1}$ | $0.9^{+0.1}_{-0.1}$ | 7.93 ± 0.06 | $25.2^{+0.1}_{-0.2}$ | $205^{+20}_{-21}$ |
| ZD6-E | 3.6067629 | −30.3809210 | 7.8802 | $1.96^{+0.07}_{-0.06}$ | $-17.5^{+0.1}_{-0.1}$ | $8.2^{+0.1}_{-0.2}$ | $0.0^{+0.2}_{-0.2}$ | <7.75[a] | <24.7 | $48^{+15}_{-15}$ |
| ZD12-W | 3.6069704 | −30.3808620 | 7.8759 | $1.96^{+0.07}_{-0.06}$ | $-19.2^{+0.1}_{-0.1}$ | $8.4^{+0.1}_{-0.2}$ | $0.7^{+0.1}_{-0.1}$ | 7.55 ± 0.06[b] | $25.7^{+0.1}_{-0.1}$ | $669^{+59}_{-62}$ |
| ZD12-E | 3.6070579 | −30.3807390 | 7.8782 | $1.96^{+0.07}_{-0.06}$ | $-18.1^{+0.1}_{-0.1}$ | $8.4^{+0.1}_{-0.1}$ | $0.3^{+0.1}_{-0.1}$ | 6.98 ± 0.04 | $25.4^{+0.1}_{-0.1}$ | $37^{+6}_{-6}$ |
| ZD3+ZD6 | 3.6065249 | −30.3808000 | 7.8799 | $1.95^{+0.07}_{-0.06}$ | $-19.9^{+0.1}_{-0.1}$ | $9.2^{+0.1}_{-0.1}$ | $1.5^{+0.1}_{-0.1}$ | 7.94 ± 0.05 | $24.5^{+0.1}_{-0.1}$ | $99^{+9}_{-10}$ |
| ZD12 | 3.6065249 | −30.3808000 | 7.8762 | $1.95^{+0.07}_{-0.06}$ | $-20.0^{+0.1}_{-0.1}$ | $9.1^{+0.1}_{-0.1}$ | $1.4^{+0.1}_{-0.1}$ | 7.44 ± 0.05 | $24.8^{+0.1}_{-0.1}$ | $61^{+5}_{-6}$ |
| ZD3+ZD6+ZD12 | 3.6065249 | −30.3808000 | 7.8784 | $1.95^{+0.07}_{-0.06}$ | $-20.8^{+0.1}_{-0.1}$ | $9.5^{+0.1}_{-0.1}$ | $1.7^{+0.1}_{-0.1}$ | 7.92 ± 0.06 | $24.5^{+0.1}_{-0.1}$ | $58^{+5}_{-6}$ |

**Notes.** Measurements are corrected for magnification (Section 2).
[a] The metallicity using the direct-T method is $\log({\rm O/H})+12 = 7.41^{+0.19}_{-0.17}$.
[b] [O II] is not detected, thus the derived metallicity via our strong-line calibration method (Section 3.2.2) is considered an upper limit.

measurements for the calibrators and iteratively evaluate the goodness of fit of the calibration for a given log(O/H). We include the measurement errors and also the scatter in the calibration from the original study at each iteration to maximally account for systematic uncertainties. The final value of log(O/H) is determined by taking the median of the distributions, and the errors are the differences to the 16th/84th percentiles. The metallicity measurements are reported in Table 2.

The indirect metallicity measurement for ZD12-W is 7.5 ± 0.1, which is consistent with the one derived with the direct-T method within the error bars. We also measure the metallicity for the two integrated systems (ZD12 and ZD3+ZD6, i.e., the yellow regions in Figure 1).

Using the calibrations presented in R. L. Sanders et al. (2024), we find similar results. However, they predict ~0.1 dex higher metallicity for ZD12. As such, our analysis and conclusion below are not affected by the choice of calibrators and line indexes.

The metallicity measurements from the R3 calibration are shown in Figure 4 by combining with stellar mass measurements obtained for the exact same defined region (see Section 3.3). The two integrated regions are located above and below the mean relation at similar redshifts (T. Morishita et al. 2024b), ~0.6 dex apart from each other. The metallicity measurements of individual [O III] regions also show large deviations, ~0.6 dex within the same galaxy, while the total measurement is represented by the region with higher metallicity. The observed scatter is discussed in Section 4.

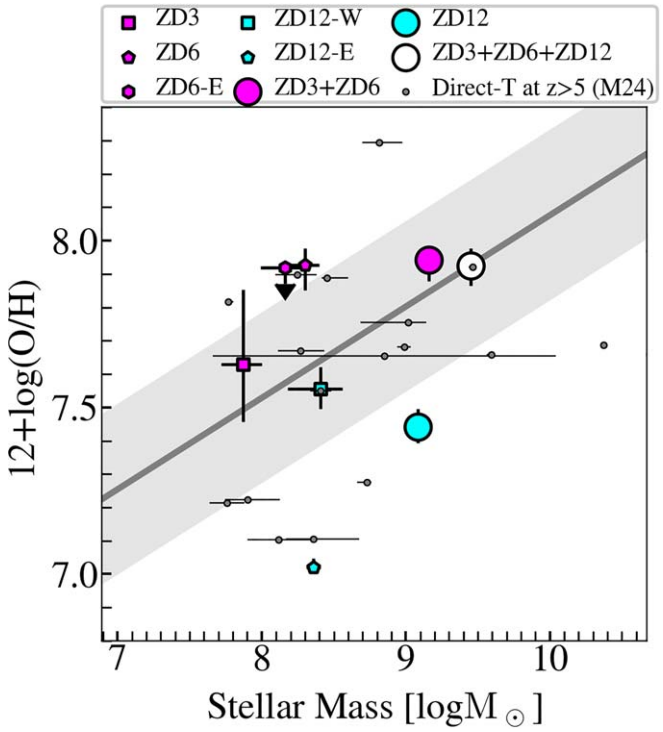


**Figure 4.** Distribution of our sample in the stellar mass–metallicity plane. Metallicities are measured using strong-line calibrations (Section 3.2.2). Large symbols are for measurements over integrated regions and small symbols for individual [O III]-emitting regions (yellow regions and cyan apertures in Figure 1, respectively). The mass–metallicity relation (T. Morishita et al. 2024b) derived for galaxies at $z > 5$ (gray dots) is shown.

### 3.3. Pixel-by-pixel SED Analysis

We infer SEDs within the detected region of our sample galaxies using the JWST+HST photometric data. First, the spatially resolved segments are defined by the Voronoi binning method (M. Cappellari & Y. Copin 2003), by requiring a minimum SNR of 5 in the F444W image. Fluxes and flux errors in each region are estimated using the PSF-matched images. We use the SED fitting code `gsf` (v1.9; T. Morishita et al. 2019), which allows flexible determinations of the SED by adopting binned star formation histories (often referred to as *nonparametric*), and adopt the SMC dust curve (K. D. Gordon et al. 2003). We follow the same procedure as described in T. Morishita et al. (2024b).

The physical quantities of each component, e.g., stellar mass and UV luminosity, are calculated by integrating the derived quantity within the defined region. The UV luminosity is corrected for dust attenuation using the $\beta_{\rm UV}$ slope, which is measured by using the posterior SED, as in R. Smit et al. (2016):

$$A_{1600} = 4.43 + 1.99\,\beta_{\rm UV}. \quad (3)$$

The attenuation-corrected UV luminosity is then converted to SFR via the relation in R. C. Kennicutt (1998):

$${\rm SFR}\,[M_\odot\,{\rm yr}^{-1}] = 1.4\times10^{-28} L_{\rm UV}\,[{\rm erg\,s^{-1}\,Hz^{-1}}]. \quad (4)$$

Since the relation is essentially for the Salpeter IMF, the estimated SFR is corrected for the Chabrier IMF by multiplying a factor of 0.63 the factor estimated from `fsps`.

By using the H$\beta$ flux in Section 3.1 and the UV luminosity derived here, we can measure the ionization photon production efficiency in each [O III]-emitting region (e.g., D. Schaerer et al. 2016; G. Prieto-Lyon et al. 2023):

$$\xi_{\rm ion} = N_{\rm LyC}/L_{\rm UV}\ [{\rm s}^{-1}/{\rm ergs}^{-1}{\rm Hz}^{-1}], \quad (5)$$

where $N_{\rm LyC}$ is the total ionizing photons of Lyman continuum, and $L_{\rm UV}$ the intrinsic UV luminosity density measured at rest-frame 1500 Å, both corrected for attenuation. Since the luminosity in the optical hydrogen recombination lines is proportional to the number of Lyman-continuum photons absorbed in the galaxy, the direct measurement of $N_{\rm LyC}$ is proportional to the ionizing photon escape fraction, $f_{\rm esc}$:

$$N_{\rm LyC} = 2.1 \times 10^{12}(1 - f_{\rm esc})^{-1} L({\rm H}\beta), \quad (6)$$

where we here adopt $f_{\rm esc} = 0$.

Similarly, using the best-fit SED, we estimate rest-frame equivalent widths (EWs) of [O III] doublet emissions. We note that continuum flux is not detected in the IFU cube in any of the [O III]-emitting regions. This means that our EW measurement is rather *indirect* and susceptible to systematics such as absolute flux calibration in the cube. However, we have validated the absolute flux accuracy by comparing the measured line fluxes with the flux excess seen in two photometric filters, F410M and F444W (where F444W captures the H$\beta$+[O III] and F410M does only continuum). The uncertainty in the continuum flux level, estimated in the SED modeling, is also added to the EW measurement uncertainties. The measurements are reported in Table 2.

## 4. Discussion

### 4.1. On the Scatter in the Metallicity Distribution

We have seen in Section 3.2 that the measured metallicity of the [O III]-emitting regions is distributed over a wide range, from $\log {\rm O/H} + 12 < 7$ to ~8 (Figure 4). Although the sample number here is small, and the strong-line calibration itself has nonnegligible scatter, the large scatter observed here is qualitatively consistent with previous studies using non-IFU spectra to derive the direct-T metallicity, reporting ~0.3 dex (e.g., T. Morishita et al. 2024b; see also Figure 4). T. Morishita et al. (2024b) attributed this partially to the elevated star formation activity in early galaxies (see below; also Section 1), but also to aperture effects from the MSA slit. Our IFU observations confirm that a large variation in metallicity is present even within single galaxy systems in these early times. This qualitatively supports the previous interpretation that the observed scatter around the mass–metallicity relation is partially due to the limited aperture size of the MSA.

Notably, the total metallicities measured in the integrated spectra are more represented by enriched components. The integrated ZD3+ZD6 system is at $\log({\rm O/H}) + 12 \sim 7.9$, whereas ZD3 is characterized with a lower metallicity, $\log({\rm O/H}) + 12 \sim 7.6$. Similarly, the integrated ZD12 system is characterized by a higher metallicity, $\log({\rm O/H}) + 12 \sim 7.4$, than ZD12-E alone, $\log({\rm O/H}) + 12 \lesssim 6.9$. This is a natural consequence of the mass–metallicity relation: that more massive regions (i.e., more luminous) outshine less enriched (fainter) regions, particularly in young galaxy systems. Interestingly, the region with the least enrichment, ZD12-E with an upper limit $\log({\rm O/H}) + 12 \lesssim 7$, is offset by ~1 kpc from the brightest region of ZD12 in NIRCam imaging. Since MSA masks are configured to source light-weighted positions by default, this presents a challenge in current MSA mask configurations in finding pristine regions of galaxies.

Although this type of observational bias is known for low-$z$ observations in the presence of mild metallicity gradients (e.g., C. A. Tremonti et al. 2004; F. Belfiore et al. 2017), the impact is likely more significant at high redshift because of the time available for chemical mixing within the ISM. T. Morishita et al. (2024b) report the redshift evolution of scatter amplitude, from ~0.1 at $z \sim 0$ (M. Curti et al. 2020) to ~0.2 at ~0.2 dex at $3 < z < 5$ and ~0.3 dex at $z > 5$ (see also M. Curti et al. 2024). The impact of star formation feedback, especially in low-mass systems of shallow potential, is therefore expected to be more significant at higher redshifts. A. Pallottini et al. (2024) show that high stochasticity in high-$z$ star formation (see also J. Mirocha & S. R. Furlanetto 2023; X. Shen et al. 2024; J. B. Muñoz et al. 2024) enables the system to exhibit large variations of metallicity, making the mass–metallicity relationship less constrained (see also Section 4.2).

On the other hand, the metallicity of ZD6 is observed to be considerably high, $\log({\rm O/H}) + 12 \sim 8$, or 10% solar. This, given the age of the Universe, ~660 Myr, suggests that metal enrichment within some subgalactic regions could be much more rapid than other regions in the same system. In particular, ZD6 is located near the center of an ongoing merger, where an accelerated gas cycle is expected. Our SED analysis of resolved pixels has revealed an increase in $A_V$, which is another evidence of fast enrichment.

As redshift increases, so does the merger rate (O. Fakhouri & C.-P. Ma 2008; V. Rodriguez-Gomez et al. 2015), and thus galaxy assembly is progressively driven by mergers rather than smooth accretion (see also T. Y.-Y. Hsiao et al. 2023; K. Boyett et al. 2024; N. Dalmasso et al. 2024; Y. Sugahara et al. 20252024, for recent observations). As a result, the chemical enrichment of the system is significantly affected by individual merger events (and also the properties of independent building blocks), rather than by smooth accretion of material and self-recycling, increasing the metallicity variation. As such, in addition to the general increase in star formation intensity in the early Universe, our study showcases that an increased fraction of merger-driven evolution would also contribute to the observed scatter in the mass–metallicity relation. A large data set of IFU observations may shed light on the relative contribution of each evolutionary channel.

### 4.2. Compact UV-bright Clumps as the Origin of Strong [O III] Emissions

The NIRSpec IFU is limited to a spatial resolution of $\sim$0.″15 ($\sim$370 pc with $\mu \sim 2$ magnification), leaving the nature of the [O III]-emitting regions rather undetermined. In the NIRCam images (Figure 1), which offer ~5× higher resolution, we see multiple UV-bright clumps in both the integrated ZD12 and ZD3+ZD6 systems, at a smaller scale than the [O III] regions. None of these clumps is detected in the F090W image, and therefore we consider that they belong to the ZD12 and ZD3 +ZD6 systems.

To study in detail these UV-bright clumps, we fit a two-dimensional light distribution in the F150W image, which corresponds to ~1700 Å rest frame, using `galfit` (C. Y. Peng et al. 2002, 2010). Each light profile of 10 UV clumps (and one

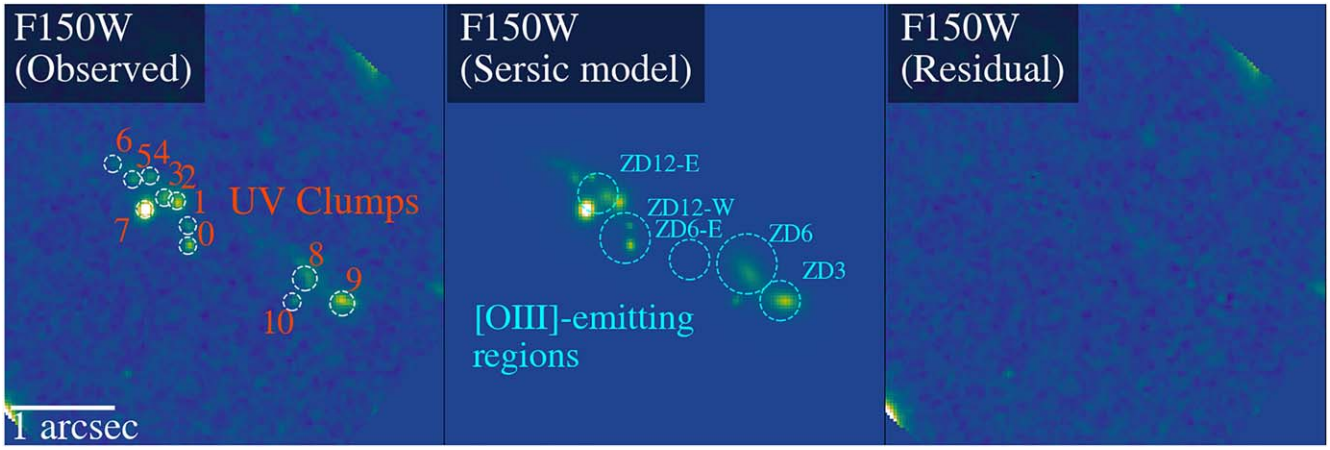


**Figure 5.** Two-dimensional light profile of the system in the NIRCam F150W band, corresponding to ~1700 Å rest frame. Clump 7 is a foreground galaxy at $z \sim 1.6$. Left: observed image; individual components fitted with `galfit` are identified (circles). Middle: modeled light profile; the [O III]-emitting regions identified in the IFU data are overlaid (cyan circles) for comparison of the relative positions. Right: residual image.

**Table 3**
Physical Properties of UV Clumps

| ID | R.A. (deg) | Decl. (deg) | $\mu$ | $m_{\rm F150W}$ (mag) | $M_{\rm UV}$ (mag) | $\log M_*$ ($M_\odot$) | $\log {\rm SFR}_{\rm UV}$ ($M_\odot {\rm yr}^{-1}$) | $\log R_e$ (kpc) | $n_{\rm Sérsic}$ | $\log \Sigma_{\rm SFR}$ ($M_\odot\,{\rm yr}^{-1}\,{\rm kpc}^{-2}$) | $\log \Sigma_*$ ($M_\odot {\rm pc}^{-2}$) |
|---|---|---|---|---|---|---|---|---|---|---|---|
| 0 | 3.60694 | −30.38082 | 1.96 | 28.3 ± 0.0 | $-17.7^{+0.1}_{-0.1}$ | $8.2^{+0.2}_{-0.2}$ | $0.5^{+0.1}_{-0.1}$ | $<-0.9$ | 0.8 ± 0.1 | >1.5 | >3.2 |
| 1 | 3.60694 | −30.38077 | 1.96 | 29.1 ± 0.2 | $-16.9^{+0.1}_{-0.1}$ | $7.9^{+0.2}_{-0.2}$ | $0.1^{+0.1}_{-0.1}$ | $<-0.9$ | 4.0 ± 2.7 | >1.1 | >2.8 |
| 2 | 3.60697 | −30.38070 | 1.96 | 27.5 ± 0.0 | $-18.4^{+0.1}_{-0.1}$ | $8.4^{+0.1}_{-0.1}$ | $0.8^{+0.1}_{-0.1}$ | −0.7 ± 0.4 | 0.8 ± 0.0 | 1.3 ± 0.4 | 3.0 ± 0.4 |
| 3 | 3.60701 | −30.38069 | 1.96 | 27.9 ± 0.1 | $-18.1^{+0.0}_{-0.0}$ | $8.5^{+0.1}_{-0.1}$ | $0.7^{+0.1}_{-0.1}$ | −0.7 ± 0.5 | 0.8 ± 0.1 | 1.2 ± 0.5 | 3.0 ± 0.5 |
| 4 | 3.60706 | −30.38063 | 1.95 | 28.8 ± 0.1 | $-17.2^{+0.0}_{-0.0}$ | $7.6^{+0.1}_{-0.1}$ | $0.1^{+0.1}_{-0.1}$ | $<-0.9$ | 0.5 ± 0.1 | >1.1 | >2.7 |
| 5 | 3.60712 | −30.38064 | 1.95 | 28.3 ± 0.2 | $-17.6^{+0.1}_{-0.1}$ | $8.2^{+0.2}_{-0.2}$ | $0.5^{+0.1}_{-0.1}$ | −0.6 ± 0.6 | 1.4 ± 0.3 | 0.9 ± 0.6 | 2.6 ± 0.6 |
| 6 | 3.60718 | −30.38060 | 1.95 | 28.5 ± 0.2 | $-17.5^{+0.1}_{-0.1}$ | $8.1^{+0.2}_{-0.2}$ | $0.5^{+0.1}_{-0.1}$ | −0.2 ± 1.0 | 1.7 ± 0.5 | 0.1 ± 1.0 | 1.7 ± 1.0 |
| 8 | 3.60656 | −30.38091 | 1.96 | 26.9 ± 0.0 | $-18.9^{+0.1}_{-0.1}$ | $8.9^{+0.1}_{-0.1}$ | $1.2^{+0.1}_{-0.1}$ | −0.3 ± 0.8 | 1.0 ± 0.0 | 0.9 ± 0.8 | 2.7 ± 0.8 |
| 9 | 3.60644 | −30.38098 | 1.97 | 27.0 ± 0.0 | $-19.0^{+0.1}_{-0.1}$ | $8.3^{+0.1}_{-0.2}$ | $0.8^{+0.1}_{-0.1}$ | −0.5 ± 0.6 | 0.7 ± 0.0 | 1.1 ± 0.6 | 2.6 ± 0.6 |
| 10 | 3.60660 | −30.38098 | 1.97 | 29.3 ± 0.0 | $-16.5^{+0.1}_{-0.1}$ | $8.0^{+0.1}_{-0.1}$ | $0.2^{+0.1}_{-0.1}$ | $<-1.0$ | 0.6 ± 0.3 | >1.4 | >3.1 |

**Note.** UV clumps are defined in the NIRCam F150W image (Figure 5). Measurements are corrected for magnification (Section 2).

foreground galaxy) is well fitted by a single Sérsic component (Figure 5). Four (0, 1, 4, and 10) have effective radii smaller than the PSF size ($\lesssim$2 pixels, or $R_e \lesssim 0\farcs06$). We consider those clumps unresolved and quote the PSF's FWHM as their upper-limit sizes. The derived physical properties of those UV clumps are reported in Table 3.

In Figure 6, we show the size distribution of the UV clumps as a function of the stellar mass. The stellar mass of each clump is estimated by using the mass-to-light ratio derived in Section 3.3 and scaling it with the total flux modeled with `galfit`. The four unresolved UV clumps are found in the regime where relatively massive clusters in the local Universe are located (M. A. Norris et al. 2014). However, at the spatial resolution available here, the detailed classification of those unresolved clumps is not possible. The other six UV clumps (2, 3, 5, 6, 8, and 9) have sizes comparable to those of individual galaxies (T. Morishita et al. 2024a).

The unresolved clumps are characterized with a high star formation surface density $\Sigma_{\rm SFR}$ (>10–100 $M_\odot\,{\rm yr}^{-1}\,{\rm kpc}^{-2}$) and surface mass surface density $\Sigma_*$ (>500–1600 $M_\odot\,{\rm pc}^{-2}$; Figure 7). The observed densities are on the upper end of individual galaxy populations at $z > 5$ (e.g., T. Morishita et al. 2024a), even reaching the realm of star clusters.

Recent observations have seen some evidence of star clusters forming in the early environment through gravitational lensing

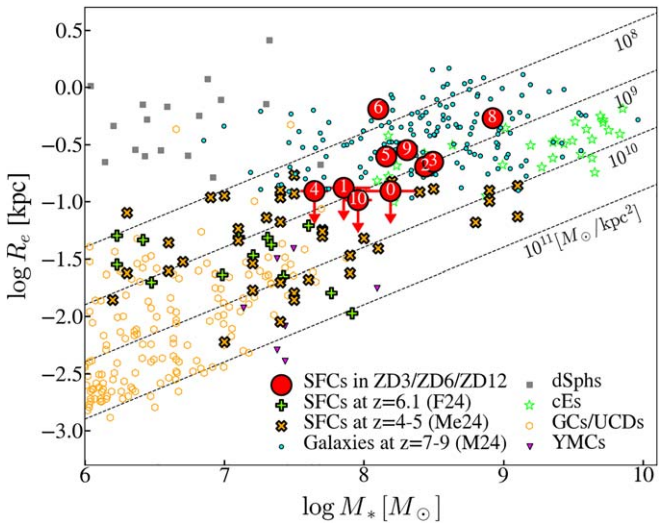


**Figure 6.** Size–mass distributions of UV-bright clumps (red circles). Half-light radii $R_e$ are measured by two-dimensional profile fitting (Figure 5). Six UV clumps (2, 3, 5, 6, 8, and 9) have sizes comparable with individual galaxies (cyan dots; T. Morishita et al. 2024a) for the given stellar mass. Four (0, 1, 4, and 10) are unresolved (upper limits), located near the boundary where local compact ellipticals (lime open stars) and ultra-compact dwarfs/globular clusters (yellow circles) are found (taken from M. A. Norris et al. 2014). For comparison, star-forming clusters within a $z = 6.1$ galaxy system (S. Fujimoto et al. 2024) and those within $z = 4$–5 galaxies (M. Messa et al. 2024) are also shown (cross symbols).

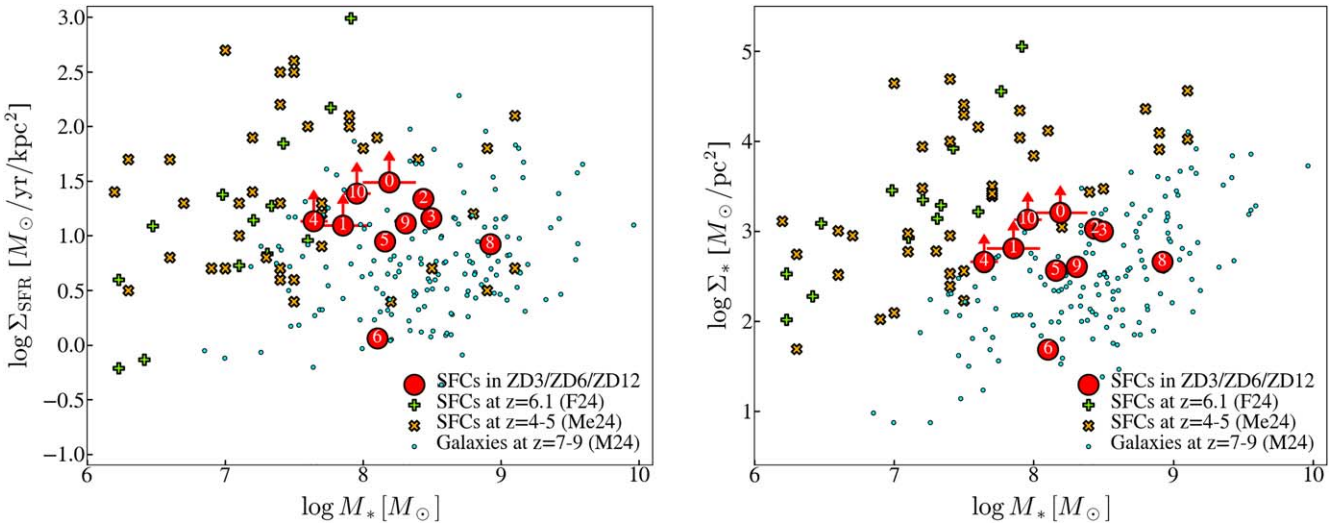


**Figure 7.** Left: star formation surface density as a function of stellar mass. Symbols are the same as in Figure 6. Right: same as the left panel but for stellar mass surface density.

(e.g., U. Meštrić et al. 2022; E. Vanzella et al. 2022, 2023a; A. Adamo et al. 2024; S. Fujimoto et al. 2024; M. Messa et al. 2024). For example, M. Messa et al. (2025) recently presented NIRSpec IFU observations and revealed star clusters of $R_e \sim 3$–$10$ pc within a strongly lensed galaxy system at $z = 6.14$. These clusters are strongly line-emitting and are characterized by blue UV slopes, $\beta_{UV} \lesssim -2.5$ and $\lesssim 0.1\,Z_\odot$.

In this context, the nature of star formation in our unresolved clumps is of particular interest. The UV clumps 0 and 1 are both located within the [O III]-emitting region (ZD12-W), one of the metal-poor regions ($\log(O/H) + 12 = 7.4$ from the direct-T method) with a high-[O III] EW, $EW_0 = 670 \pm 60$ Å. Remarkably, the measured ionizing photon production efficiency (Section 3.3) for ZD12-W is considerably high, with $\log \xi_{ion} = 25.7$ Hz erg$^{-1}$ for its $M_{UV}$ when compared to those from the literature (e.g., E. Vanzella et al. 2024). Using the linear relation between $\xi_{ion}$ and $M_{UV}$ derived by G. Prieto-Lyon et al. (2023), a rather moderate efficiency, ~25.4, would be expected for ZD12-W's $M_{UV}$. This suggests a higher escape fraction in ZD12-W than assumed here, i.e., $f_{esc} \sim 0.5$ would be required to meet the expected $\xi_{ion}$. Alternatively, if the observed H$\beta$ originates mainly in one of the two UV clumps (which have $M_{UV} \sim -17.7$ and –16.9 mag), it would make the deviation smaller, but still not completely gone.

Star formation in such dense environments plays a crucial role in chemical enrichment and may be responsible for the diverse properties observed among our samples. Recent JWST studies have also illuminated the origin of star clusters by identifying nitrogen-rich ISM in the early Universe (e.g., M. Stiavelli et al. 2025; M. W. Topping et al. 2024). A detailed study of the chemical compositions within those UV clumps would thus give us further insight into their nature, i.e., whether they are giant star-forming clumps (similar to those at lower redshifts) or even smaller-scale populations such as star clusters.

Theoretical studies have investigated the nature of star-forming clumps seen at high redshifts in relation to metallicity. K. Sugimura et al. (2024) show that a high gas density can be reached within an environment of metal-poor star formation because of the intense far-UV radiation field therein. This is qualitatively consistent with the nature of ZD12-W, with its low metallicity, high electron density, and high surface densities. Y. Nakazato et al. (2024) show that short-lived, UV-bright clumps can form through mergers, which may also be relevant to the case of the ZD3+ZD6+ZD12 system. Similarly, C. Marconcini et al. (2024a) investigated the moderate anticorrelation between $\Sigma_{SFR}$ and log(O/H) seen in the galaxy system CR7. These authors attribute it to the inflow of pristine gas, which would lower the metallicity and trigger intense star formation, though the system's global metallicity is much more enriched ($\log(O/H) + 12 \sim 8$) than our case here. Different mechanisms responsible for high $\Sigma_{SFR}$ may be in action in different metallicity regimes.

### 4.3. Revisiting A2744-z7p9OD as a Protocluster

Lastly, we revisit the characterization of A2744-z7p9OD as a protocluster system. A2744-z7p9OD was reported in T. Morishita et al. (2023) for the spectroscopic confirmation of seven member galaxies at $z = 7.88$ (see also G. Roberts-Borsani et al. 2022). The following studies identified two (YD1, s1; T. Hashimoto et al. 2023) and one (ZD4; Z. Chen et al. 2024) additional members. With the new addition of ZD12 in this study, now 11 member galaxies have been confirmed (Figure 1), distributed within a small projected region ($r \sim 60$ pkpc in the source plane) and redshift slice ($\delta_z = 0.019$, or ~25 pMpc). Following T. Morishita et al. (2023), we here aim to estimate the overdensity factor, the total halo mass, and the system velocity dispersion.

The overdensity factor, defined as $\delta = (n - \bar{n})/\bar{n}$, represents the excess of the surface number density from the field average. We use $R = 60$ pkpc, which defines the extent of the member galaxies in the source plane, and a redshift slice of $\delta_z = 0.019$. One of the member galaxies, s1, is excluded from the calculation, as this source is rather considered as a subregion and does not qualify for a "galaxy" count. For field reference, we use the luminosity function at $z \sim 8$ presented in R. J. Bouwens et al. (2021) and integrate it down to $M_{UV} \sim -17.4$ mag, the lowest magnitude among the confirmed member galaxies (except for s1). For the area within $R = 60$ pkpc, we expect $\bar{n} = 0.2^{+0.5}_{-0.4}$ galaxies in average fields. With the reference number for the average field, we find

$\delta = 44^{+89}_{-31}$ for A2744-z7p9OD, where the uncertainties quoted represent Poisson noise.

To estimate the total halo mass of A2744-z7p9OD, we estimate the halo mass of the individual components from the halo mass–galaxy luminosity relation (C. A. Mason et al. 2023). Using the relation and adding the halo mass estimates of all confirmed members, we obtain a total halo mass estimate of $5.8^{+0.2}_{-0.3} \times 10^{11}\,M_{\odot}$, but this is likely a lower limit given that there are photometrically selected candidates which are not spectroscopically followed.

In addition, we can take advantage of the spectroscopic data to obtain an estimate of the velocity dispersion for the whole system. We adopt a simple Gaussian estimator and bootstrap method to derive the uncertainty (T. C. Beers et al. 1990), obtaining $1100 \pm 500\,\mathrm{km\,s^{-1}}$, consistent with the original estimate in T. Morishita et al. (2023). We caution the reader that the system is likely not virialized, and that in computing this quantity we are assuming the spread in redshift with respect to the mean is due to motion as opposed to distance along the line of sight.

We note that the only Ly$\alpha$-emitting member galaxy, ZD4 (Z. Chen et al. 2024), is located in an off-core region of the protocluster (Figure 1).

## 5. Summary

In this study, we reported our JWST/NIRSpec IFU observations of a merging galaxy system in the core of A2744-z7p9OD at $z = 7.88$, the most distance protocluster to date. The IFU cube revealed five [O III]-emitting regions, including those from a newly confirmed protocluster member, ZD12. We found large scatters in the measured metallicity in those emitting regions for ~1 dex. We discussed the origin of the large scatter and attributed it to a fast gas cycle from intense star formation and merger-driven growth. The presence of large variations in metallicity, even within a single galaxy (~0.6 dex), posed a challenge to current slit spectroscopy with NIRSpec/MSA in finding metal-poor star formation in the early Universe (e.g., those found in E. Vanzella et al. 2023b), and also in obtaining the *true* metallicity of a given galaxy system, due to the limited aperture size of the MSA.

We have seen that ZD12 consists of multiple UV-bright clumps, revealed in the high-resolution NIRCam F150W image. Four of these are unresolved and characterized with high masses or star formation surface densities. Two unresolved UV clumps are likely responsible for the strong [O III] in ZD12-W, which is characterized by a metal-poor ISM ($\log(\mathrm{O/H}) + 12 = 7.4$), high electron density ($n_e = 2200^{+6700}_{-1600}$), large [O III] EW ($\mathrm{EW}_0 = 670 \pm 60$ Å), and high ionizing photon efficiency ($\log \xi_{\mathrm{ion}} = 25.7\,\mathrm{Hz\,erg^{-1}}$). The nature of those compact star-forming clumps remains undetermined. For this, detailed chemical investigations that involve other element species, such as nitrogen and argon, would be required (e.g., M. Stiavelli et al. 2025).

Lastly, we revisited the characterization of A2744-z7p9OD as a large-scale structure. Its overdensity factor, halo mass, and velocity dispersion have been updated by including the newly identified ZD12 and other new member galaxies in the literature; however, we note that our characterization was made with measurements within the very central core of the protocluster, and the membership determination is still incomplete because of the nature of the existing observations. Extending the search for member galaxies to further distances and different wavelengths (e.g., submillimeter range for heavily obscured sources) will provide us with a more comprehensive view of the protocluster.

## Acknowledgments

We thank Abdurro'uf for sharing the compiled data catalog of electron density measurements in the literature. We thank the anonymous referee for the careful reading of the manuscript and constructive comments. Some/all of the data presented in this paper were obtained from the Mikulski Archive for Space Telescopes (MAST) at the Space Telescope Science Institute (STScI). The specific observations analyzed can be accessed via doi:10.17909/q8cd-2q22. We acknowledge support for this work under NASA grant No. 80NSSC22K1294. T.M. received support from NASA through the STScI grant Nos. HST-GO-17231 and JWST-GO-3990. Support for this work was provided by NASA through the NASA Hubble Fellowship grant No. HST-HF2-51492 awarded to A.J.S. by the STScI, which is operated by the Association of Universities for Research in Astronomy, Inc., for NASA, under contract NAS5-26555. A.J.S. also received support from NASA through the STScI grant Nos. HST-GO-16773 and JWST-GO-2974.

*Software:* Astropy (Astropy Collaboration et al. 2013, 2018; Astropy Collaboration et al. 2022), `gsf` (T. Morishita et al. 2019), `lacosmic` (P. G. van Dokkum 2001; L. Bradley 2023), numpy (C. R. Harris et al. 2020), python-fsps (D. Foreman-Mackey et al. 2014), JWST pipeline (H. Bushouse et al. 2023), `SExtractor` (E. Bertin & S. Arnouts 1996).

## ORCID iDs

Takahiro Morishita https://orcid.org/0000-0002-8512-1404
Massimo Stiavelli https://orcid.org/0000-0001-9935-6047
Eros Vanzella https://orcid.org/0000-0002-5057-135X
Pietro Bergamini https://orcid.org/0000-0003-1383-9414
Kristan Boyett https://orcid.org/0000-0003-4109-304X
Marco Chiaberge https://orcid.org/0000-0003-1564-3802
Claudio Grillo https://orcid.org/0000-0002-5926-7143
Nicha Leethochawalit https://orcid.org/0000-0003-4570-3159
Matteo Messa https://orcid.org/0000-0003-1427-2456
Guido Roberts-Borsani https://orcid.org/0000-0002-4140-1367
Piero Rosati https://orcid.org/0000-0002-6813-0632
Anowar J. Shajib https://orcid.org/0000-0002-5558-888X

## References

Abdurro'uf, Larson, R. L., Coe, D., et al. 2024, ApJ, 973, 47
Adamo, A., Bradley, L. D., Vanzella, E., et al. 2024, Natur, 632, 513
Andrews, B. H., & Martini, P. 2013, ApJ, 765, 140
Arribas, S., Perna, M., Rodrìguez Del Pino, B., et al. 2024, A&A, 688, A146
Astropy Collaboration, Price-Whelan, A. M., Lim, P. L., et al. 2022, ApJ, 935, 167
Astropy Collaboration, Price-Whelan, A. M., Sipőcz, B. M., et al. 2018, AJ, 156, 123
Astropy Collaboration, Robitaille, T. P., Tollerud, E. J., et al. 2013, A&A, 558, A33
Beers, T. C., Flynn, K., & Gebhardt, K. 1990, AJ, 100, 32
Belfiore, F., Maiolino, R., Tremonti, C., et al. 2017, MNRAS, 469, 151
Bergamini, P., Acebron, A., Grillo, C., et al. 2023a, A&A, 670, A60
Bergamini, P., Acebron, A., Grillo, C., et al. 2023b, ApJ, 952, 84
Bertin, E., & Arnouts, S. 1996, A&AS, 117, 393
Bezanson, R., Labbe, I., Whitaker, K. E., et al. 2024, ApJ, 974, 92
Bouwens, R. J., Oesch, P. A., Stefanon, M., et al. 2021, AJ, 162, 47
Boyett, K., Trenti, M., Leethochawalit, N., et al. 2024, NatAs, 8, 657
Bradley, L. 2023, larrybradley/lacosmic: 1.1.0, Zenodo, doi:10.5281/zenodo.10145563

Bushouse, H., Eisenhamer, J., Dencheva, N., et al. 2023, JWST Calibration Pipeline, v1.10.0, Zenodo, doi:10.5281/zenodo.7795697
Calzetti, D., Armus, L., Bohlin, R. C., et al. 2000, ApJ, 533, 682
Cappellari, M., & Copin, Y. 2003, MNRAS, 342, 345
Chabrier, G. 2003, PASP, 115, 763
Chemerynska, I., Atek, H., Dayal, P., et al. 2024, ApJL, 976, L15
Chen, W., Kelly, P., Morishita, T., et al. 2022, TNSAN, 166, 1
Chen, Z., Stark, D. P., Mason, C., et al. 2024, MNRAS, 528, 7052
Chisholm, J., Tremonti, C., & Leitherer, C. 2018, MNRAS, 481, 1690
Curti, M., Mannucci, F., Cresci, G., & Maiolino, R. 2020, MNRAS, 491, 944
Curti, M., Maiolino, R., Curtis-Lake, E., et al. 2024, A&A, 684, A75
Dalmasso, N., Calabrò, A., Leethochawalit, N., et al. 2024, MNRAS, 533, 4472
Fakhouri, O., & Ma, C.-P. 2008, MNRAS, 386, 577
Foreman-Mackey, D., Sick, J., & Johnson, B. 2014, python-fsps: Python bindings to FSPS v0.1.1, Zenodo, doi:10.5281/zenodo.12157
Fujimoto, S., Ouchi, M., Kohno, K., et al. 2024, arXiv:2402.18543
Fukugita, M., Ichikawa, T., Gunn, J. E., et al. 1996, AJ, 111, 1748
Gallazzi, A., Charlot, S., Brinchmann, J., White, S. D. M., & Tremonti, C. A. 2005, MNRAS, 362, 41
Gordon, K. D., Clayton, G. C., Misselt, K. A., Landolt, A. U., & Wolff, M. J. 2003, ApJ, 594, 279
Harris, C. R., Millman, K. J., van der Walt, S. J., et al. 2020, Natur, 585, 357
Hashimoto, T., Álvarez-Márquez, J., Fudamoto, Y., et al. 2023, ApJL, 955, L2
Heintz, K. E., Brammer, G. B., Giménez-Arteaga, C., et al. 2023, NatAs, 7, 1517
Hsiao, T. Y.-Y., Coe, D., Abdurro'uf, et al. 2023, ApJL, 949, L34
Ishigaki, M., Ouchi, M., & Harikane, Y. 2016, ApJ, 822, 5
Isobe, Y., Ouchi, M., Nakajima, K., et al. 2023, ApJ, 956, 139
Izotov, Y. I., Stasińska, G., Meynet, G., Guseva, N. G., & Thuan, T. X. 2006, A&A, 448, 955
Jones, G. C., Bowler, R., Bunker, A. J., et al. 2024, arXiv:2412.15027
Kelly, P. L., Diego, J. M., Rodney, S., et al. 2018, NatAs, 2, 334
Kennicutt, R. C. 1998, ApJ, 498, 541
Kirby, E. N., Cohen, J. G., Guhathakurta, P., et al. 2013, ApJ, 779, 102
Lamperti, I., Arribas, S., Perna, M., et al. 2024, A&A, 691, A153
Laporte, N., Streblyanska, A., Clement, B., et al. 2014, A&A, 562, L8
Laseter, I. H., Maseda, M. V., Curti, M., et al. 2024, A&A, 681, A70
Li, S., Wang, X., Chen, Y., et al. 2025, ApJL, 979, L13
Lotz, J. M., Koekemoer, A., Coe, D., et al. 2017, ApJ, 837, 97
Ma, X., Hopkins, P. F., Faucher-Giguère, C.-A., et al. 2016, MNRAS, 456, 2140
Mannucci, F., Cresci, G., Maiolino, R., Marconi, A., & Gnerucci, A. 2010, MNRAS, 408, 2115
Marconcini, C., D'Eugenio, F., Maiolino, R., et al. 2024a, arXiv:2411.08627
Marconcini, C., D'Eugenio, F., Maiolino, R., et al. 2024b, MNRAS, 533, 2488
Mason, C. A., Trenti, M., & Treu, T. 2023, MNRAS, 521, 497
Merlin, E., Bonchi, A., Paris, D., et al. 2022, ApJL, 938, L14
Messa, M., Dessauges-Zavadsky, M., Adamo, A., Richard, J., & Claeyssens, A. 2024, MNRAS, 529, 2162
Messa, M., Vanzella, E., Loiacono, F., et al. 2025, A&A, 694, A59
Meštrić, U., Vanzella, E., Zanella, A., et al. 2022, MNRAS, 516, 3532
Mirocha, J., & Furlanetto, S. R. 2023, MNRAS, 519, 843
Morishita, T., & Stiavelli, M. 2023, ApJL, 946, L35
Morishita, T., Abramson, L. E., Treu, T., et al. 2019, ApJ, 877, 141
Morishita, T., Roberts-Borsani, G., Treu, T., et al. 2023, ApJL, 947, L24
Morishita, T., Stiavelli, M., Chary, R.-R., et al. 2024a, ApJ, 963, 9
Morishita, T., Mason, C. A., Kreilgaard, K. C., et al. 2025, ApJ, 983, 152
Morishita, T., Stiavelli, M., Grillo, C., et al. 2024b, ApJ, 971, 43
Morishita, T., Liu, Z., Stiavelli, M., et al. 2025, ApJ, 982, 153
Muñoz, J. B., Mirocha, J., Chisholm, J., Furlanetto, S. R., & Mason, C. 2024, MNRAS, 535, L37
Naidu, R. P., Matthee, J., Kramarenko, I., et al. 2024, arXiv:2410.01874
Nakajima, K., Ouchi, M., Isobe, Y., et al. 2023, ApJS, 269, 33
Nakazato, Y., Ceverino, D., & Yoshida, N. 2024, ApJ, 975, 238
Norris, M. A., Kannappan, S. J., Forbes, D. A., et al. 2014, MNRAS, 443, 1151
Oke, J. B., & Gunn, J. E. 1983, ApJ, 266, 713
Oppenheimer, B. D., & Davé, R. 2006, MNRAS, 373, 1265
Osterbrock, D. E. 1989, Astrophysics of Gaseous Nebulae and Active Galactic Nuclei (Mill Valley, CA: Univ. Science Books),
Pallottini, A., Ferrara, A., Gallerani, S., et al. 2024, arXiv:2408.00061
Peng, C. Y., Ho, L. C., Impey, C. D., & Rix, H.-W. 2002, AJ, 124, 266
Peng, C. Y., Ho, L. C., Impey, C. D., & Rix, H.-W. 2010, AJ, 139, 2097
Postman, M., Coe, D., Benítez, N., et al. 2012, ApJS, 199, 25
Prieto-Lyon, G., Strait, V., Mason, C. A., et al. 2023, A&A, 672, A186
Rigby, J. R., Vieira, J. D., Phadke, K. A., et al. 2025, ApJ, 978, 108
Roberts-Borsani, G., Morishita, T., Treu, T., et al. 2022, ApJL, 938, L13
Rodriguez-Gomez, V., Genel, S., Vogelsberger, M., et al. 2015, MNRAS, 449, 49
Sanders, R. L., Shapley, A. E., Kriek, M., et al. 2016, ApJL, 825, L23
Sanders, R. L., Shapley, A. E., Topping, M. W., Reddy, N. A., & Brammer, G. B. 2024, ApJ, 962, 24
Schaerer, D., Izotov, Y. I., Verhamme, A., et al. 2016, A&A, 591, L8
Scholtz, J., Curti, M., D'Eugenio, F., et al. 2025, MNRAS, 539, 2463
Senchyna, P., Plat, A., Stark, D. P., & Rudie, G. C. 2024, ApJ, 966, 92
Shen, X., Borrow, J., Vogelsberger, M., et al. 2024, MNRAS, 527, 2835
Smit, R., Bouwens, R. J., Labbé, I., et al. 2016, ApJ, 833, 254
Steinhardt, C. L., Jauzac, M., Acebron, A., et al. 2020, ApJS, 247, 64
Stiavelli, M., Morishita, T., Chiaberge, M., et al. 2023, ApJL, 957, L18
Stiavelli, M., Morishita, T., Chiaberge, M., et al. 2025, ApJ, 981, 136
Suess, K. A., Weaver, J. R., Price, S. H., et al. 2024, ApJ, 976, 101
Sugahara, Y., Álvarez-Márquez, J., Hashimoto, T., et al. 2025, ApJ, 981, 135
Sugimura, K., Ricotti, M., Park, J., Garcia, F. A. B., & Yajima, H. 2024, ApJ, 970, 14
Topping, M. W., Stark, D. P., Senchyna, P., et al. 2024, MNRAS, 529, 3301
Tremonti, C. A., Heckman, T. M., Kauffmann, G., et al. 2004, ApJ, 613, 898
Treu, T., Roberts-Borsani, G., Bradac, M., et al. 2022, ApJ, 935, 110
Tumlinson, J., Peeples, M. S., & Werk, J. K. 2017, ARA&A, 55, 389
van Dokkum, P. G. 2001, PASP, 113, 1420
Vanzella, E., Castellano, M., Bergamini, P., et al. 2022, ApJL, 940, L53
Vanzella, E., Claeyssens, A., Welch, B., et al. 2023a, ApJ, 945, 53
Vanzella, E., Loiacono, F., Bergamini, P., et al. 2023b, A&A, 678, A173
Vanzella, E., Loiacono, F., Messa, M., et al. 2024, A&A, 691, A251
Zheng, W., Shu, X., Moustakas, J., et al. 2014, ApJ, 795, 93